28th Symposium on Naval Hydrodynamics
Pasadena, California, 12-17 September 2010

Numerical Simulation of Strong Free-Surface Turbulence for Mechanistic Study

Yi Liu, Xin Guo, Di Yang, and Lian Shen*
(Department of Civil Engineering, The Johns Hopkins University, USA)

Abstract

We perform a simulation based study of strong free-surface turbulence (SFST) aiming at a fundamental understanding of the flow physics. Using hybrid Eulerian simulation, we obtain finely-resolved turbulence and wave fields as the database for systematic analysis. Different flow regimes are demonstrated by the representative instantaneous surface geometries. Surface elevation spectra show significant difference among flows with different gravity and surface tension effects. Volume fraction in the air–water mixed flow, turbulent velocity fluctuation, and phase averaged Reynolds stress are quantified. Instantaneous flow structures that affect the surface geometry and the turbulence statistics are discussed. Dissipation and turbulence transportation induced by surface breaking are demonstrated, and the enhancement effect on the turbulence beneath is elucidated. We also use a decomposition scheme to distinguish the wave and turbulence effects. The results of this study may be useful for the development of improved turbulence models for SFST and steep/breaking waves (SBW).

1 INTRODUCTION

Modeling of violent free-surface turbulent flows, which is of vital importance to many naval applications, requires a deep understanding of the fundamental physics of SFST. The interaction of turbulence with surface waves is complex in many ways. For example, the turbulence can be substantially distorted by the periodic orbital motion and the surface drift associated with the waves. Wave breaking is an important source of turbulence in upper ocean and near naval structures. On the other hand, the turbulence scatters and dissipates surface waves. The turbulence pressure and shear stress may also amplify waves and trigger wave breaking (Guo & Shen, 2010).

The complex surface processes pose great challenges to the simulation of SFST. For direct numerical simulation (DNS), the violent surface motion makes the kinematic and dynamic boundary conditions difficult to represent in numerical schemes (cf. the discussion in Shen, 2007). For large-eddy simulation (LES), besides the question of the applicability of subgrid-scale (SGS) models originally developed for other flows (Shen & Yue, 2001), the multiphase nature of SFST also introduces issues in the formulation of LES itself. For example, new filters based on component-weighted, volume-averaging procedure are required; commutativity between filter and derivative needs to be accounted for; and additional interfacial SGS terms need to be modeled (Reboux, Sagaut & Lakehal, 2006; Labourasse et al. 2007; Liovic & Lakehal, 2007).

Accurate simulation and prediction of free-surface turbulent flows requires high-fidelity numerical schemes and innovative analysis and modeling approaches. Recently, we combined the strengths of state-of-the-art level set (LS) method, volume of fluid (VOF) method, and ghost fluid (GF) method to develop a hybrid simulation capability for SFST. We also developed a scheme to identify wave and turbulence components in the flow (Guo & Shen, 2009). This decomposition helps us understand the different roles that wave and turbulence play in interfacial processes. It also elucidates the modulation dynamics of waves by SFST and the distortion mechanism of turbulence by large-amplitude surface waves.

*Email address for correspondence: LianShen@jhu.edu.

2 PROBLEM SETUP AND NUMERICAL APPROACH

2.1 Setup of numerical simulation

We consider the simulation of a canonical free-surface and turbulence interaction problem (Fig.1) with DNS method. In this simulation, turbulence is generated in the deep water and is then transported to the free surface to interact with the surface. The air part is initially quiescent and its motion is driven by the water side. Because of the very small air-to-water density ratio, the influence of air on the water motion is relatively weak, and the motion of the free surface is mainly generated by the turbulence in the water.

To obtain steady free-surface turbulence statistics, we choose a forced turbulence field in the deep water as the turbulence source. We adopt a linear forcing method (Lungren, 2003; Rosales & Meneveau, 2005) to generate quasi-steady isotropic homogeneous turbulence. In this method, a body force proportional to the turbulent velocity is added to the momentum equations:

$$\frac{\partial \vec{u}}{\partial t}+\vec{u}\cdot\nabla\vec{u}=\frac{1}{\rho}(-\nabla p+\nabla\cdot\tau+\rho\vec{g}+\sigma\kappa\delta(\vec{x}_s)+c_0F(z_c)\vec{u}'). \tag{1}$$

Here $\vec{u}$ is the velocity vector; $\vec{u}'$ is the velocity fluctuation. Since there is no mean flow in this problem, $\vec{u}'=\vec{u}$. And ρ is the density; p is the pressure; $\tau=\mu(\nabla\vec{u}+\nabla\vec{u}^T)$ is the shear stress tensor; μ is the dynamic viscosity; $\vec{g}$ is the gravitational acceleration; σ is the surface tension coefficient; κ is the surface curvature; $\vec{x}_s$ denoted the surface location; $\delta(x)$ is the Dirac delta function; z_c is the vertical coordinate with its origin located at the center of the water domain; $F(z_c)$ is the forcing distribution function; c_0 is the forcing coefficient. The function $F(z_c)$ has the form

$$F(z_c)=\begin{cases} 1, & z_c\le l_b, \text{ bulk region,}\\ \frac{1}{2}\left(1-\cos\left[\frac{\pi}{l_d}(z_c-l_b-l_d)\right]\right), & \\ \qquad l_b<z_c\le l_b+l_d, & \text{damping region,}\\ 0, & z_c>l_b+l_d, \text{ free region,}\end{cases} \tag{2}$$

which is symmetric about the origin $z_c=0$. The forcing coefficient c_0 is prescribed and it determines the strength of the turbulence generated.

With the linear forcing, steady isotropic and homogeneous turbulence is generated at the center of the forcing region. The turbulence is then transported upward from the deep water to the free surface to disturb the surface and generate waves, dimples, scars, and even spays and bubbles.

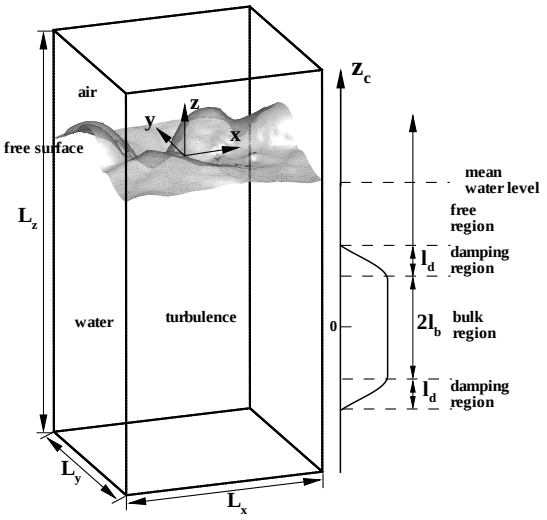

Figure 1: Sketch of the multi-phase flow simulation setup of the free-surface turbulence problem.

2.2 Simulation parameters

After non-dimensionalization with a length scale L, velocity scale U and the density of water ρ_w, the Navier-Stokes equations become

$$\begin{aligned}\frac{\partial\tilde{\vec{u}}}{\partial\tilde{t}}+\tilde{\vec{u}}\cdot\tilde{\nabla}\tilde{\vec{u}} &= -\frac{\tilde{\nabla}\tilde{p}}{\tilde{\rho}}+\frac{1}{Re}\frac{1}{\tilde{\rho}}\tilde{\nabla}\cdot\tilde{\tau}+\frac{1}{Fr^2}\vec{k}\\ &\quad+\frac{1}{We}\frac{1}{\tilde{\rho}}\tilde{\kappa}\delta(\tilde{\vec{x}}_s)+\tilde{c}_0F(\tilde{z_c})\tilde{\vec{u}}'.\end{aligned} \tag{3}$$

Here all quantities with tilde are non-dimensionalized (hereafter we omit the tilde for simplicity); $\vec{k}$ is the unit vector in the gravity direction; $Re=UL/\nu$ is the Reynolds number; $Fr=\sqrt{U^2/gL}$ is the Froude number; $We=\rho U^2L/\sigma$ is the Weber number. The dimensionless domain size is $L_x\times L_y\times L_z=2\pi\times 2\pi\times 6.5\pi$ and the mean water level is at $z=5\pi$.

In the free surface–turbulence interaction process, gravity and surface tension play an important role in stabilizing the surface from the disturbance of the turbulence beneath. Let q denote the turbulence velocity fluctuation magnitude and l the turbulence integral scale. According to Brocchini & Peregrine (2001), the influence of gravity and surface tension can be characterized by four flow regimes in the $q-l$ space as: weak turbulence regime, surface tension dominated regime, gravity dominated

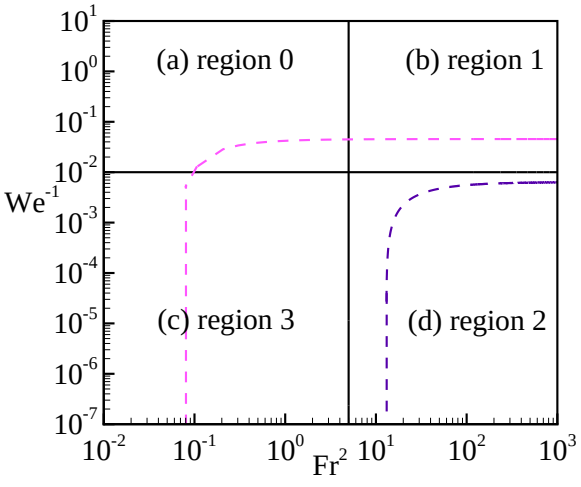

Figure 2: Diagram of the flow regimes in the $Fr-We$ space. Region 0: weak turbulence regime; region 1: surface tension dominated regime; region 2: very strong turbulence regime; region 3: gravity dominated regime. The region between the two dash lines represents the marginal breaking region obtained by Brochini & Peregrine (2001).

regime, and very strong turbulence regime. After non-dimensionalization, the effects of gravity and surface tension are represented by Fr and We, respectively. In this study, $Re = 1000$ and $c_0 = 0.1$ are fixed. We map the four flow regimes in the $Fr-We$ space as shown in Fig.2. The marginal breaking region is marked by two colored dash lines.

2.3 Numerical approach

In this study, we develop a coupled LS/VOF/GF approach. Being a front capturing Eulerian method using an LS function, it handles surface pinching off and reconnection naturally on Eulerian grid, which facilitates the simulation of SFST and SBW.

In the LS method (Sussman, Smereka and Osher 1994; Sussman et al. 1998), the free surface is represented implicitly by the signed distance (LS) function (Fig.3)

$$\phi(\vec{x},t) = \begin{cases} d & \text{in water,} \\ 0 & \text{on surface,} \\ -d & \text{in air.} \end{cases} \tag{4}$$

Here d is the distance from point $\vec{x}$ to the free surface.

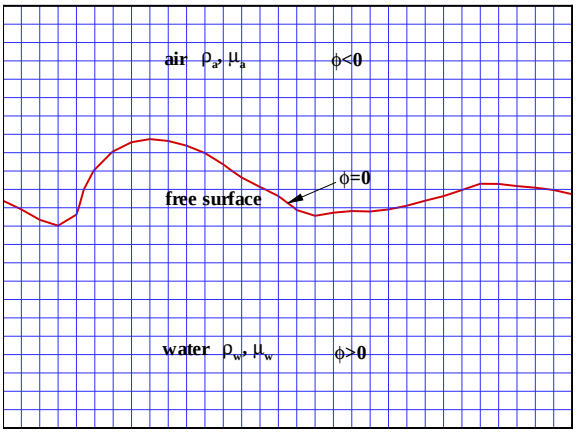

Figure 3: Sketch of the level set function.

The LS function is advected by the flow:

$$\frac{\partial \phi}{\partial t} + \vec{u} \cdot \nabla \phi = 0. \tag{5}$$

The above equation cannot guarantee the signed distance property of the LS function as time evolves, and a reinitialization procedure is needed. The following equation

$$\frac{\partial \phi_c}{\partial \tau} + sign(\phi)(|\nabla \phi_c| - 1) = 0 \tag{6}$$

is used to correct ϕ. Here τ is artificial time. Initial condition is $\phi_c(\vec{x},0) = \phi(\vec{x})$. After Eqn. 6 is solved to a steady state, ϕ takes the value of ϕ_c.

Using ϕ, the surface normal vector and the curvature are calculated as

$$\vec{n} = \frac{\nabla \phi}{|\nabla \phi|}, \tag{7}$$

and

$$\kappa = \nabla \cdot \vec{n} = \nabla \cdot \frac{\nabla \phi}{|\nabla \phi|}. \tag{8}$$

The density and viscosity in the multi-fluid flow field are written as

$$\begin{cases} \rho(\phi) = \rho_w H(\phi) + \rho_a (1 - H(\phi)), \\ \mu(\phi) = \mu_w H(\phi) + \mu_a (1 - H(\phi)). \end{cases} \tag{9}$$

Here ρ_w, ρ_a and μ_w, μ_a are the densities and viscosities of water and air, respectively; $H(x)$ is the Heaviside step function.

The Navier-Stokes equations for air and wa-

ter are now written as one equation

$$\begin{aligned}\frac{\partial \vec{u}}{\partial t}+\nabla\cdot(\vec{u}\vec{u}) &= -\frac{1}{\rho(\phi)}\nabla p+\frac{1}{Re}\frac{1}{\rho(\phi)}\nabla\cdot(2\mu(\phi)\bar{D})\\ &\quad+\frac{1}{Fr^2}\vec{k}+\frac{1}{We}\frac{1}{\rho(\phi)}\kappa\delta(\phi)\vec{n}\\ &\quad+c_0F(z_c)\vec{u}'.\end{aligned} \tag{10}$$

Here $\bar{D}=\frac{1}{2}(\nabla\vec{u}+\nabla\vec{u}^T)$ is the strain rate tensor.

To improve the mass conservation, the VOF method is coupled with the LS method (Sussman and Puckett, 2000). The following VOF equation

$$\frac{\partial F}{\partial t}+\vec{u}\cdot\nabla F=0 \tag{11}$$

is solved together with the LS equation. Here F is the volume fraction of water in each computational cell. Since F has a sharp jump across the interface, the above equation cannot be discretized directly. Instead, the interface is reconstructed through a piecewise linear interface construction (PLIC) method and is used to calculate the volume flux in Eq.11 (Rider & Kothe, 1998). The VOF method uses the surface normal calculated from the LS function to reconstruct the surface and the VOF function is used to correct the LS function at the interface (Fig.4).

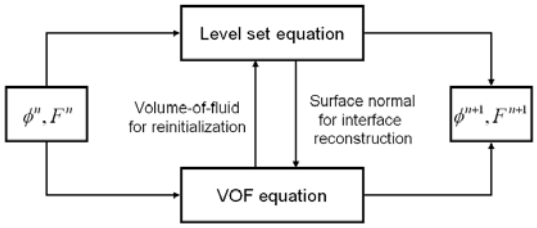

Figure 4: Schematics of the coupled LS and VOF method

The GF method (Kang, Fedkiw and Liu 2000; Liu, Fedkiw and Kang 2000) is incorporated to treat the interface in a sharp fashion. It captures the boundary conditions at the contact discontinuity without numerical smearing. The following interface jump condition

$$\left[\begin{pmatrix}\vec{N}\\ \vec{T}_1\\ \vec{T}_2\end{pmatrix}(p\mathbf{I}-\tau)\vec{N}^T\right]=\begin{pmatrix}\sigma\kappa\\ 0\\ 0\end{pmatrix} \tag{12}$$

is implemented. Here $\vec{N}$ is the unit normal vector of the free surface; $\vec{T}_1$ and $\vec{T}_2$ are the two unit tangent

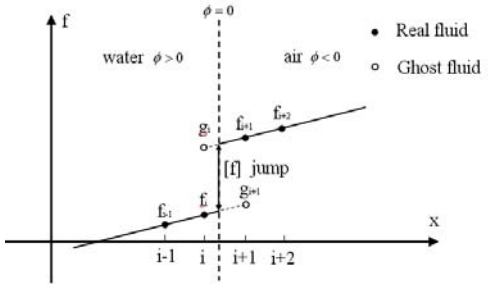

(a)

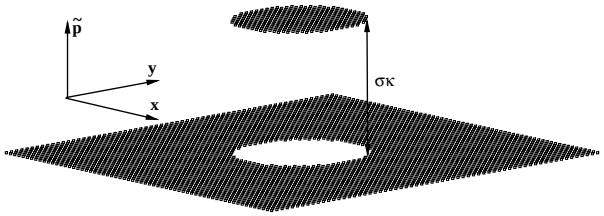

(b)

Figure 5: (a) Sketch of GF method. (b) Pressure distribution of a static bubble in water without gravity effect calculated by GF method.

vectors; $[\,\cdot\,]$ denotes the jump across the interface. Combined with the continuity condition at the interface, the above jump condition is rewritten as the stress jump condition

$$\begin{aligned}&\begin{pmatrix}[\mu u_x] & [\mu u_y] & [\mu u_z]\\ [\mu v_x] & [\mu v_y] & [\mu v_z]\\ [\mu w_x] & [\mu w_y] & [\mu w_z]\end{pmatrix}=\\ &[\mu]\begin{pmatrix}\nabla u\\ \nabla v\\ \nabla w\end{pmatrix}\begin{pmatrix}\vec{0}\\ \vec{T}_1\\ \vec{T}_2\end{pmatrix}^T\begin{pmatrix}\vec{0}\\ \vec{T}_1\\ \vec{T}_2\end{pmatrix}\\ &+[\mu]\vec{N}^T\vec{N}\begin{pmatrix}\nabla u\\ \nabla v\\ \nabla w\end{pmatrix}\vec{N}^T\vec{N}\\ &-[\mu]\begin{pmatrix}\vec{0}\\ \vec{T}_1\\ \vec{T}_2\end{pmatrix}^T\begin{pmatrix}\vec{0}\\ \vec{T}_1\\ \vec{T}_2\end{pmatrix}\begin{pmatrix}\nabla u\\ \nabla v\\ \nabla w\end{pmatrix}\vec{N}^T\vec{N},\end{aligned} \tag{13}$$

and the pressure jump condition

$$[p]=2[\mu](\nabla u\cdot\vec{N},\nabla v\cdot\vec{N},\nabla w\cdot\vec{N})\cdot\vec{N}+\sigma\kappa. \tag{14}$$

With the gravity terms absorbed to the pressure, the

dynamic pressure jump condition becomes

$$[p] = 2[\mu](\nabla u \cdot \vec{N}, \nabla v \cdot \vec{N}, \nabla w \cdot \vec{N}) \cdot \vec{N} + \sigma\kappa + [\rho]gz. \quad (15)$$

The stress and pressure jump conditions are then treated with the GF method. In Fig.5, the pressure field of a static bubble in the water is simulated with the GF method, the sharp pressure jump induced by the surface tension is presented.

The incorporation of the GF method prevents numerical contamination due to density, viscosity, and surface tension smoothing in the traditional LS method. With this hybrid approach, the interfacial flow structure is accurately captured, which provides valuable information on the physics of the free-surface flow.

3 RESULTS

3.1 Free surface disturbed by turbulence

We first discuss the geometrical characteristics of the free surface, which is disturbed by the turbulence underneath. The aforementioned four flow regimes have substantially different appearance in the instantaneous free surface.

Weak turbulence regime

In this regime (region 0 in Fig.2a), turbulence disturbance to the free surface is relatively weak because of the large gravity and surface tension stabilizing effects. The free surface appears flat and smooth, as shown in Fig. 6(a) where instantaneous elevation contours for the case of ($Fr^2 = 0.8, We = 40$) are plotted. For flows in this regime, the dynamic and kinematic free surface boundary conditions can be linearized to simplify the simulation, and analysis of one phase fluid is often performed.

Surface tension dominated regime

In this regime (region 1 in Fig.2b), the surface tension effect is strong and the gravity effect is weak. The cohesion of the water is maintained by the surface tension, and the surface is smooth. Because the gravity effect is small, it cannot keep the surface flat. As a result, the surface has a smooth round shape (Fig.6b), which is called "knobbly" by Brocchini & Peregrine (2001).

Gravity dominated regime

This regime (region 3 in Fig.2c) is the most common one that is often observed in oceans, lakes, and rivers. Due to the gravity effect, if the turbulence is not strong enough, the surface cannot have very large deformation. But small scale surface structures such as dimples, scars, and waves are often present. In Fig.6(c), an instantaneous surface for the case of ($Fr^2 = 4, We = \infty$) is shown. A scar is observed on the left corner, and some dimples also exist nearby.

Very strong turbulence regime

In this flow regime (region 2 in Fig.2d), both the gravity and surface tension effects are weak. The motion at the free surface is violent, and the surface cannot keep flat or smooth. The turbulence can bring the water to a significant height and make the surface break. Large amount of spays and air entrainments may occur. The region near the surface becomes a air-water mixture. In Fig.6(d), an instantaneous surface for the case of ($Fr^2 = 32, We = 1$) is shown. At this moment, the surface geometry is quite complex. The surface elevation cannot be described by a single-value function because the surface is multi-connected. Water jet shoots up and reenters the water later, playing an important role in the atmosphere–ocean exchange of mass, momentum, and energy.

3.2 Surface spectra

Having illustrating the instantaneous surface elevation, we next present its spectral statistics, which is again quite different under different gravity and surface tension effects. Surface tension has more influence on small scale surface structures because of their relatively large curvature. The surface spectra of a gravity dominated case and a surface tension dominated case are plotted in Fig.7(a) and Fig.7(b), respectively. For the former, the surface spectrum has a slope of $k^{-2.5}$. For the latter, high wavenumber components are damped by the strong surface tension, and the surface spectrum has a much steeper slope of $k^{-5.5}$.

3.3 Surface wave and roughness

When the free surface is disturbed by the turbulence from below, it can respond passively and locally in the form of surface roughness. The energy received

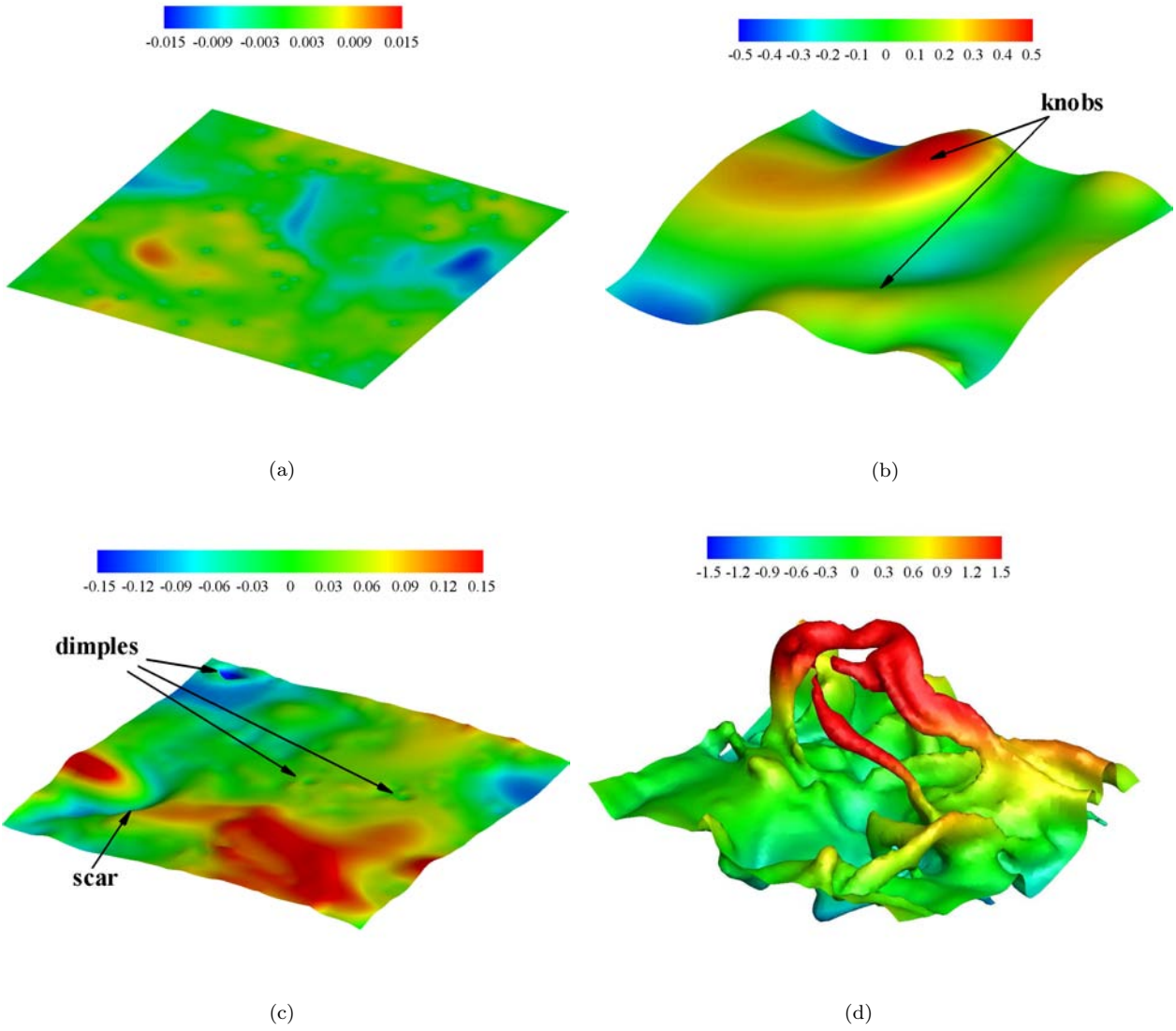

Figure 6: Instantaneous free surface elevation for the cases of: (a) ($Fr^2 = 0.8$, $We = 40$) that is in the weak turbulence regime, (b) ($Fr^2 = 128$, $We = 40$) that is in the surface tension dominated regime, (c) ($Fr^2 = 4$, $We = \infty$) that is in the gravity dominated regime, and (d) ($Fr^2 = 32$, $We = \infty$) that is in the very strong turbulence regime.

can also propagate away in the form of surface waves.

The normalized frequency–wavenumber spectrum of the surface elevation (Guo & Shen, 2010)

$$\Phi_\eta^N(|\vec{k}|,\omega) = \frac{1}{(2\pi)^3(\eta_{rms})^2} \cdot \int_T \int_S \overline{\eta(\vec{x},t)\eta(\vec{x}+\vec{r},t+\tau)} e^{-i(\vec{k}\cdot\vec{r}+\omega\tau)} d\vec{r}d\tau \tag{16}$$

is used to study the free surface waves and roughness. Here T is sampling duration; S is the horizontal plane; ω is the temporal frequency; $|\vec{k}|$ is the module of the horizontal wavenumber vector.

In Fig.8, $\Phi_\eta^N(|\vec{k}|,\omega)$ for the weak turbulence case of ($Fr^2 = 0.8, We = 40$) is plotted. Two ridges are observed. One is represented by the solid line in the figure, which corresponds to the dispersion relationship of capillary–gravity waves

$$\omega = \sqrt{\frac{k}{Fr^2} + \frac{k^3}{We}}. \tag{17}$$

The other denotes the characteristic frequency of the

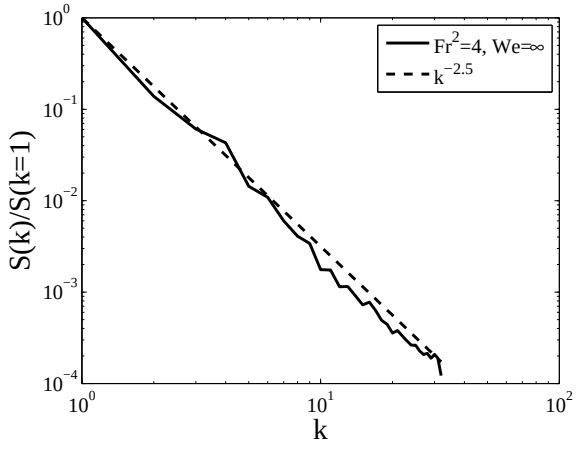

(a)

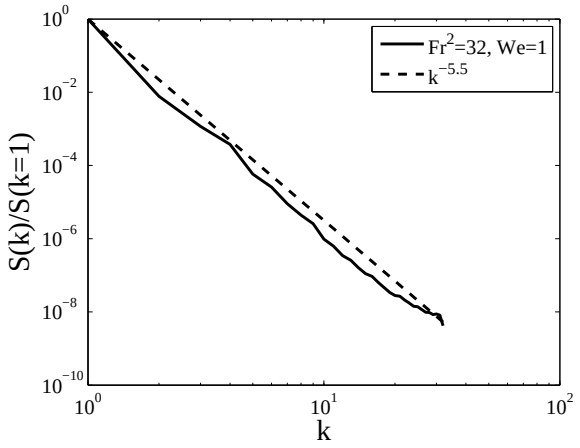

(b)

Figure 7: Surface elevation spectra of (a) the gravity dominated case of ($Fr^2 = 4$, $We = \infty$) and (b) the surface tension dominated case of ($Fr^2 = 32$, $We = 1$).

surface elevation at each wavenumber (the dash-dot line in Fig.8)

$$\omega = \sqrt{\frac{\Phi_\eta(k)}{\Phi_{\eta_t}(k)}}. \tag{18}$$

Here Φ_η and Φ_{η_t} are the one-dimensional spatial spectra of the surface elevation and its time derivative, respectively. The lower ridge corresponds to the turbulence induced roughness. It extends to high wavenumbers, indicating that the turbulence roughness is dominant at small spatial scales. Its time scale is also much smaller than the wave period.

If the linearized free-surface kinematic boundary condition (KBC) $\eta_t = w$ is used, Eq.19

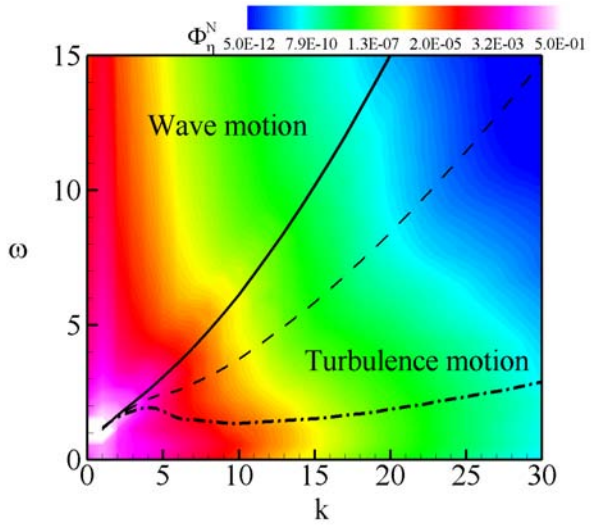

Figure 8: Normalized frequency–wavenumber spectrum of the surface elevation for the weak turbulence case of ($Fr^2 = 0.8, We = 40$).

becomes the one used by Borue et al. (1995)

$$\omega = \sqrt{\frac{\Phi_\eta(k)}{\Phi_w(k)}}. \tag{19}$$

It is plotted as the dashed line in Fig.8. It deviates from the ridge, suggesting that the nonlinearity plays an important role in the dynamics of surface roughness.

3.4 Intermittency

For very violent free surfaces with surface breaking such as the case of ($Fr^2 = 32, We = \infty$), using surface elevation to describe the free surface is no longer appropriate because it is multiple-valued. The flow near the surface is often an air–water mixture. The water phase is the focus of our study here. We define the phase indicator as

$$I = \begin{cases} 1 & \text{water}, \\ 0 & \text{air}. \end{cases} \tag{20}$$

After averaging, the phase indicator becomes the intermittency factor

$$\gamma(z) = < I(x, y, z, t) > . \tag{21}$$

It is also the averaged volume fraction of water, which is an important quantity in the modeling of multiphase turbulent flows.

In Fig.9(a), we plot the intermittency factor with respect to the water depth for cases with different Froude and Weber numbers. Among different cases, the intermittency factors have different lengths of extension but a similar shape. It is found that their shape can be fitted by the complementary error function erfc(z).

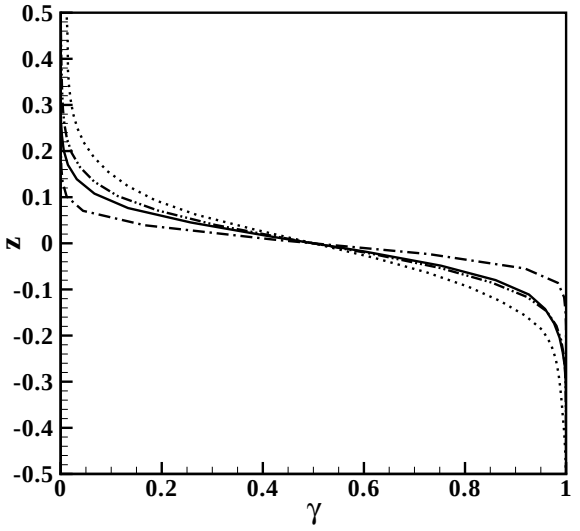

(a)

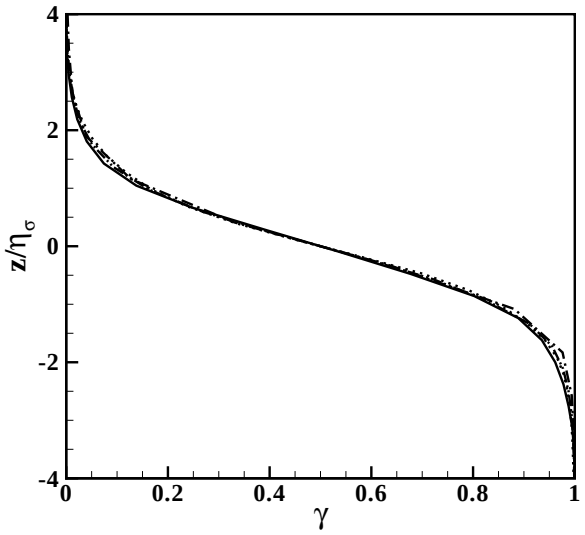

(b)

Figure 9: (a) Intermittency factors of the cases with violent free surfaces: · · · · · · , ($Fr^2 = 32, We = \infty$); – · · – · · – , ($Fr^2 = 32, We = 500$); —— , ($Fr^2 = 32, We = 40$); – · – · – , ($Fr^2 = 8, We = \infty$); (b) intermittency factors with z normalized by the equivalent thickness η_σ.

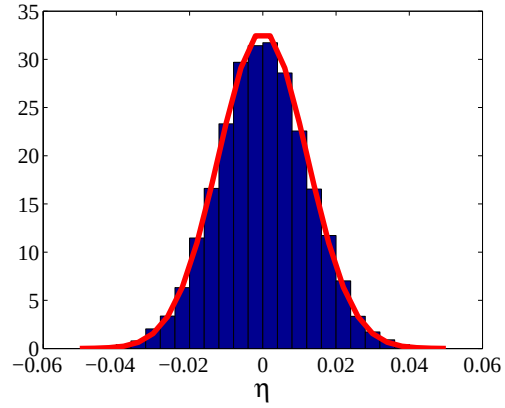

(a)

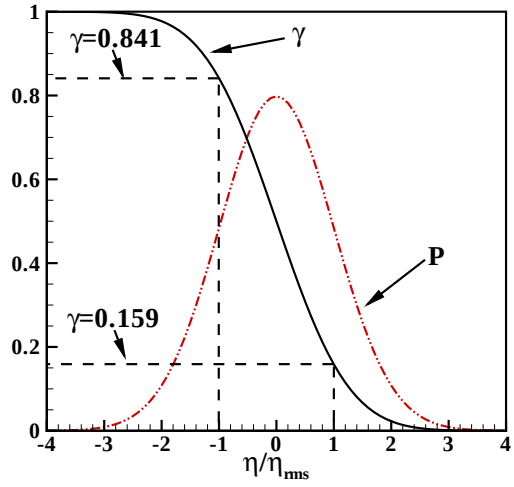

(b)

Figure 10: (a) Histogram of the surface elevation of the mild surface case of ($Fr^2 = 32, We = 1$) and the fitted Gaussian function. (b) Relationship between intermittency factors and the surface elevation probability density function.

We define the intermittency layer thickness based on an analogy to the η_{rms} of mild surface cases. Here η_{rms} denotes the root-mean-square of the surface elevation. We plot the histogram of the surface elevation for the mild surface case of ($Fr^2 = 32, We = 1$) in Fig.10(a). It fits the Gaussian function well. Therefore, we express the probability density function of η as

$$P(\eta = z) = \frac{1}{\sqrt{2\pi\eta_{rms}^2}} e^{-z^2/2\eta_{rms}^2}. \qquad (22)$$

The intermittency factor is calculated as

$$\begin{aligned}\gamma(z) &= 1-\int_{-\infty}^{z} P(z')dz' \\ &= 1-\int_{-\infty}^{0} P(z')dz' - \int_{0}^{z} P(z')dz' \\ &= 0.5-0.5\mathrm{erf}(z/\sqrt{2}\eta_{rms}) \\ &= 0.5\mathrm{erfc}(z/\sqrt{2}\eta_{rms}).\end{aligned} \tag{23}$$

We have $\gamma(z=\eta_{rms}) \approx 0.159$ and $\gamma(z=-\eta_{rms}) \approx 0.841$. These values are case independent. We have

$$\eta_{rms} = (z|_{\gamma=0.159} - z|_{\gamma=0.841})/2. \tag{24}$$

Analogically, we define the intermittency layer thickness for cases with violent surfaces as

$$\eta_{\sigma} = (z|_{\gamma=0.159} - z|_{\gamma=0.841})/2. \tag{25}$$

After z is normalized by η_{σ}, lines plotted in Fig.9(a) almost become a single line (Fig.9(b)).

The intermittency layer thickness for cases with different Froude numbers but the same Weber number $We=\infty$ is plotted in Fig.11(a). A straight line through the origin fits the data. The linear fitting can be explained by the balance between the turbulent kinetic energy (TKE) and the gravity potential energy (surface tension energy is zero since $We=\infty$), which can be described as

$$\frac{1}{2}q^2\eta_{\sigma} \sim \frac{\eta_{\sigma}^2}{2Fr^2}. \tag{26}$$

As a result, $\eta_{\sigma}/(2Fr^2)$ is comparable to $q^2/2$, which is about the same for all cases.

The intermittency layer thickness is also plotted in Fig.11(b) with respect to $1/We$ for cases with the same Froude number $Fr^2=32$. The larger the Weber number, the thicker the intermittency layer. But a linear relationship between the thickness and the Weber number does not exist, because the gravity effect still exists in these cases. In other words, the energy balance is among TKE, gravity potential energy, and surface tension energy. The ratio between the gravity potential energy and the surface tension energy is not a constant, and the surface elevation is also affected by the surface curvature $1/\kappa$ through the surface tension energy. Therefore, simple relationship between η_{σ} and $1/We$ does not exist in Fig.11(b).

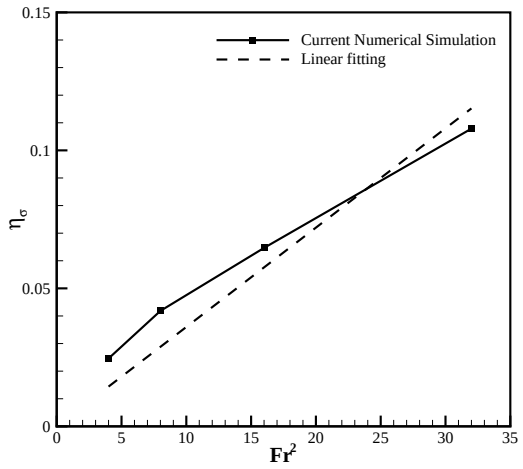

(a)

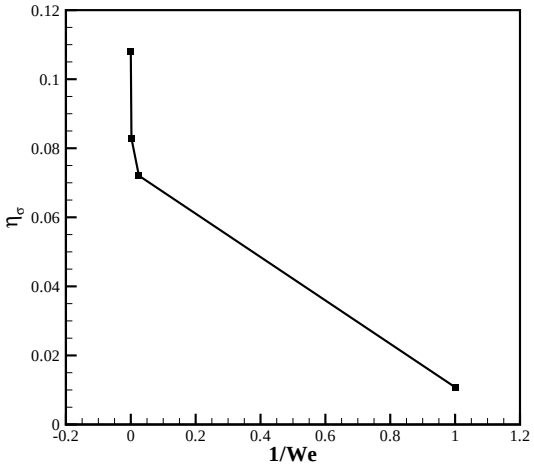

(b)

Figure 11: Intermittency layer thickness for cases with: (a) the same Weber number $We=\infty$ but different Froude numbers; (b) the same Froude number $Fr^2=32$ but different Weber numbers.

3.5 Turbulence statistics

3.5.1 Horizontal velocity fluctuation u'

In Fig.12, the vertical profiles of the horizontal velocity fluctuations u' for different cases are plotted. The velocity fluctuations are normalized by the corresponding value at the water depth $z=-0.5$.

In Fig.12(a), the profiles of u' for cases with the same Weber number $We=\infty$ but different Froude numbers are plotted. The u' is smaller for cases with larger Froude numbers. For the case of $Fr^2=1$, u' increases significantly when approaching the mean water level. In Fig.12(b), u' for cases with the same Froude number $Fr^2=32$ but different Weber numbers is plotted. At the surface, u' is

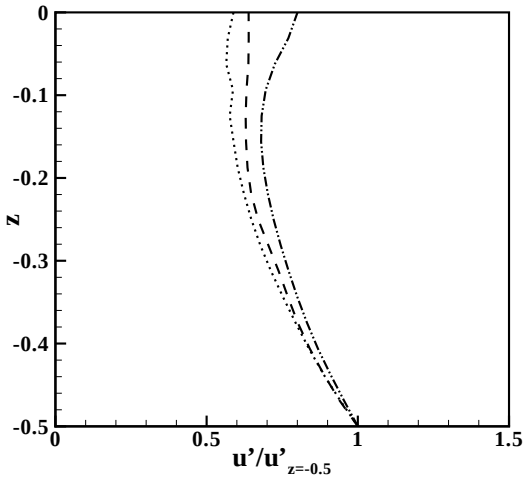

(a)

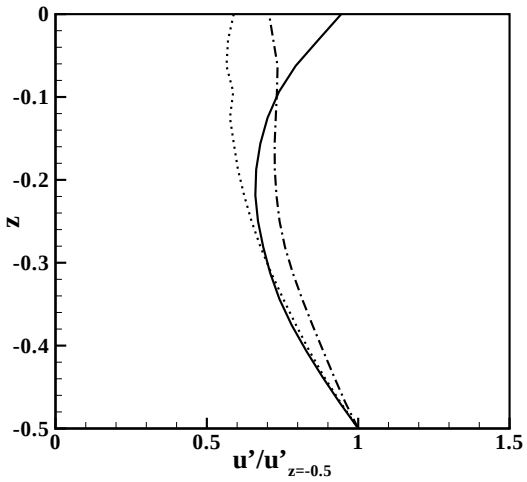

(b)

Figure 12: Horizontal velocity fluctuations of cases with (a) the same Weber number $We = \infty$ but different Froude numbers: $\cdots\cdots$ $Fr^2 = 32$; $- - -$ $Fr^2 = 4$; $- \cdot - \cdot - \cdot -$ $Fr^2 = 1$, (b) the same Froude number $Fr = 32$ but different Weber numbers: $\cdots\cdots$ $We = \infty$; $- \cdot - \cdot -$ $We = 40$; —— $We = 1$.

smaller for cases with larger Weber numbers. Similar to the case of ($Fr^2 = 1$, $We = \infty$), u' for the case of ($Fr^2 = 32$, $We = 1$) increases towards the free surface. For cases where the surface elevation is small, the strong blockage effect turns the vertical motion into horizontal directions. The smaller the Weber number and Froude number, the larger the blockage effect. Therefore, the flow in region 0 (weak turbulence) has the largest blockage effect and the flow in region 2 has the weakest blockage effect.

3.5.2 Vertical velocity fluctuation w'

The vertical velocity fluctuation w' as a function of water depth is plotted in Fig.13. In general, w' shows the opposite trend as u' does when the Froude and Weber numbers change. This is because the vertical motion is blocked by the free surface and its energy is transferred to the horizontal motion when the surface is approached. It is also interesting that for the case of ($Fr^2 = 32, We = \infty$), the vertical velocity fluctuation even increases slightly as the water surface is approached from below, because the blockage effect is countered by the turbulence generation due to strong surface breaking (Fig.6(d)).

3.5.3 Phase averaged Reynolds stress

The phase averaged turbulent normal Reynolds stress $< u'u'I >$ and $< w'w'I >$ are plotted in Figs.14 and 15, respectively. The phase averaged Reynolds stress is determined by both the turbulence intensity and the intermittency. Above the mean water level, the intermittency factor is small. The phase averaged Reynolds stress is mainly determined by the intermittency factor, and they thus have the similar shape. At lower heights, the fluid is mainly of water phase, and as expected, the $< u'u'I >$ and $< w'w'I >$ have the similar behavior as the turbulence velocity fluctuations discussed earlier.

3.6 Flow structures

To further understand the turbulence statistics, we next investigate flow structures. It is found that events such as splat and surface breaking play an important role.

3.6.1 Splat and antisplat

When an fluid element moves towards a surface, the surface blockage effect turns the motion from the surface normal direction to the outward horizontal ones that are radially along the surface, a process called splat. When the radial flows from different splats encounter each other, the flow may be forced to return to the bulk flow, a process called antisplat. For the

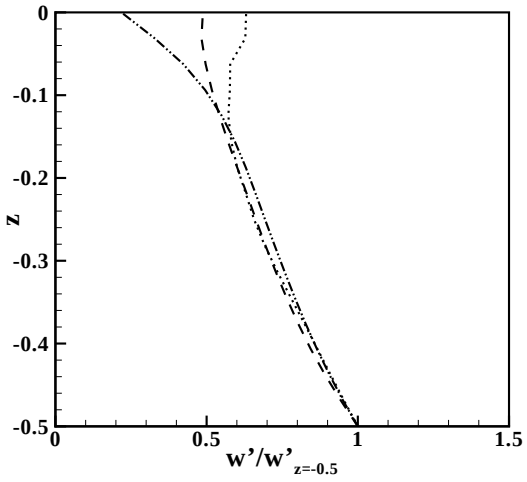

(a)

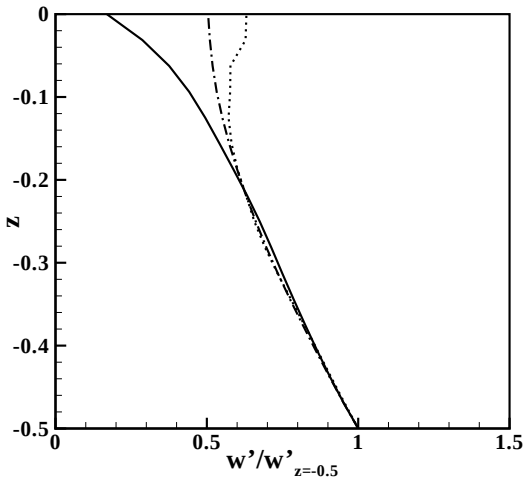

(b)

Figure 13: Vertical velocity fluctuations of cases with (a) the same Weber number $We = \infty$ but different Froude numbers, (b) the same Froude number $Fr^2 = 32$ but different Weber number. (See Fig.12 for line legend.)

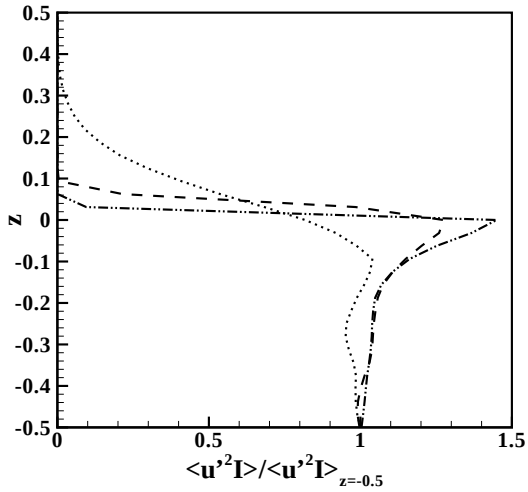

(a)

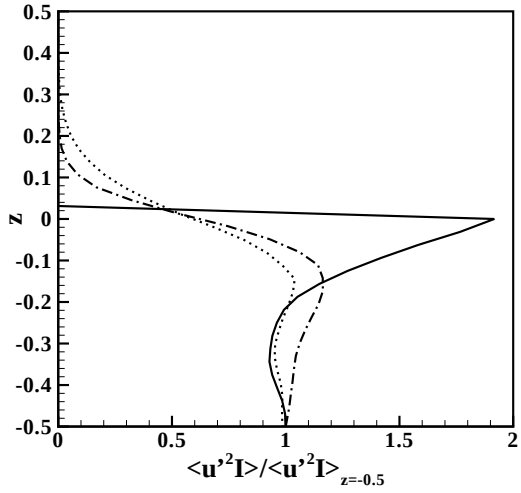

(b)

Figure 14: Phase weighted horizontal turbulent normal stress $< u'u'I >$ of cases with (a) the same Weber number $We = \infty$ but different Froude numbers; (b) the same Froude number $Fr^2 = 32$ but different Weber numbers. (See Fig.12 for line legend.)

free-surface problems, the surface blockage is caused by the gravity and surface tension effects.

In Fig.16(a), a horizontal slice near the free surface for the case of ($Fr^2 = 32$, $We = 1$) is plotted with horizontal velocity vectors and vertical velocity contours. Three splats can be seen in the region with large positive vertical velocity and radial horizontal velocity vectors. Antisplats are located at the edge of the splat with negative vertical velocity. The antisplat regions are long and thin.

A vertical cut through a splat is plotted in Fig.16(b), the dynamic pressure contours show a high pressure region where the flow hits the surface. On the sides of this splat, two counter rotating vortices are formed because of the radial flow motion.

The vortex structures presented in Fig.16(c) by the iso-surface of the second eigenvalue λ_2 of the

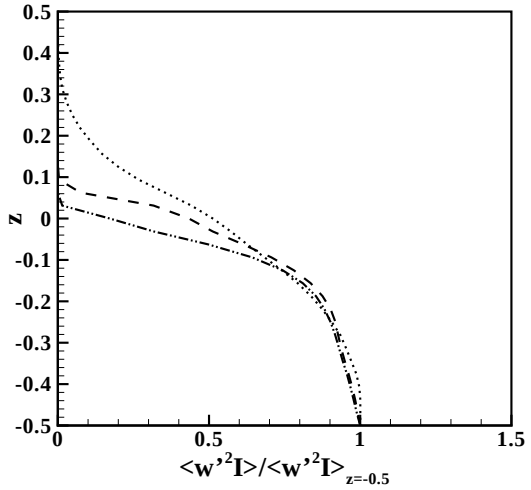

(a)

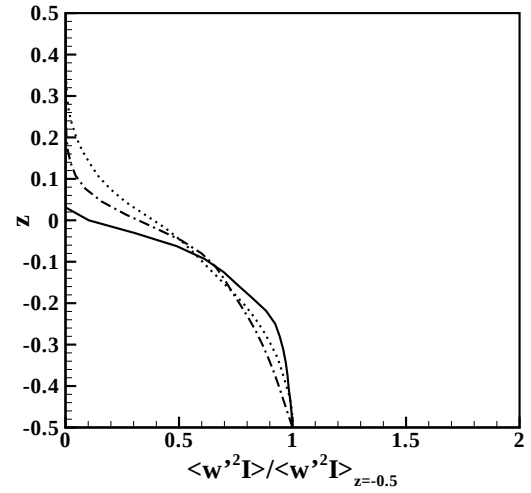

(b)

Figure 15: Phase weighted vertical turbulent normal stress $< w'w'I >$ of cases with (a) the same Weber number $We = \infty$ but different Froude numbers; (b) the same Froude number $Fr^2 = 32$ but different Weber numbers. (See Fig.12 for line legend.)

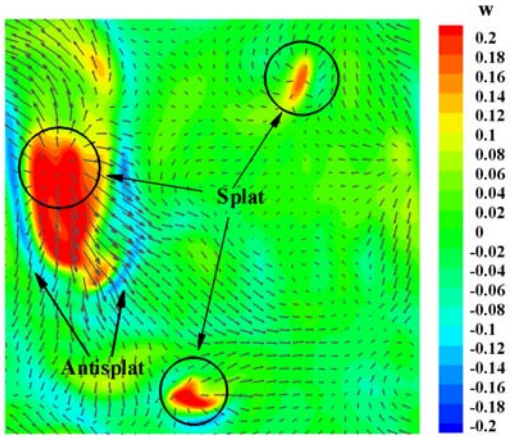

(a)

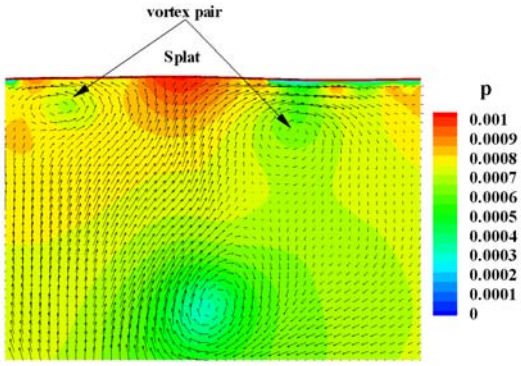

(b)

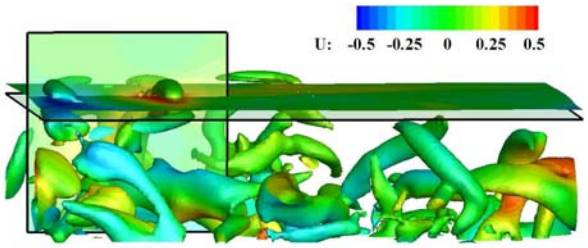

(c)

Figure 16: Instantaneous flow structures of the case of $(Fr^2 = 32, We = 1)$: (a) horizontal slice close to the interface; (b) vertical slice through a splat; (c) free surface and vortex structures.

velocity gradient tensor show vortex tubes parallel to the free surface. There are also airside vortex structures generated because of the radial motion on the free surface.

For the strong turbulence cases, the surface is so violent that splat can be found directly from the surface geometry. In Fig.17(a), we plot an instantaneous free surface and velocity vectors for the case of $(Fr^2 = 32,\ We = \infty)$. In this figure, a large dome-like surface geometry is located at the center of the surface, which is the result of a large splat there. We also plot the vertical velocity contours on a vertical cut through the dome-like geometry. Strong upward motion exists in the dome (Fig.17b), which eventually breaks the dome and brings the fluid to a significant

height (plotted in Fig.6d).

Splat also plays an important role in turbulence stress and energy transport. In Fig.17(c) and Fig.17(d), the transport of horizontal and vertical normal stress on the vertical cut through the splat are plotted. In the dome area, there is strong positive vertical transport, meaning that velocity fluctuations associated with the splat transports kinetic energy toward the surface.

3.6.2 Breaking surface

Strong splats bring water blobs to a significant height and generate surface breaking. When a breaking occurs, the surface sheet overturns, reenters the water, splashes, and entrains a large amount of air. For very strong turbulence cases (large Froude number and Weber number), surface breaking is a common phenomenon. In Fig.18, a surface breaking process is presented.

When the water sheet impinges on the water surface below, there exists strong shear in the contacting region. The shear causes high dissipation rate of the kinetic energy. In Fig.19(a), the distribution of energy dissipation on a vertical cut is presented. Large dissipation in the contacting region is clearly shown. Surface breaking also enhances Reynolds stress transport. In Fig.19(b), the horizontal transport of the horizontal normal stress is plotted. When the water sheet reenters, the strong shear brings a large amount of horizontal normal stress into the water.

3.7 Decomposition of wave and turbulence motions

We apply Helmholtz decomposition to the flow field as

$$\vec{u} = \vec{u}_{wave} + \vec{u}_{turb}. \tag{27}$$

Here $\vec{u}_{wave}$ is the irrotational flow field representing the wave motion, and $\vec{u}_{turb}$ is the remaining solenoidal flow field representing the turbulence motion. In Fig.20, the decomposed flow field for the case of ($Fr^2 = 0.8$, $We = 40$) is plotted. Wave motion mainly exists close to the free surface. It is small in magnitude compared with the turbulence motion because the wave amplitude is relatively small in this case.

As an example of the effect of wave motion on turbulence, the production of Reynolds stress from

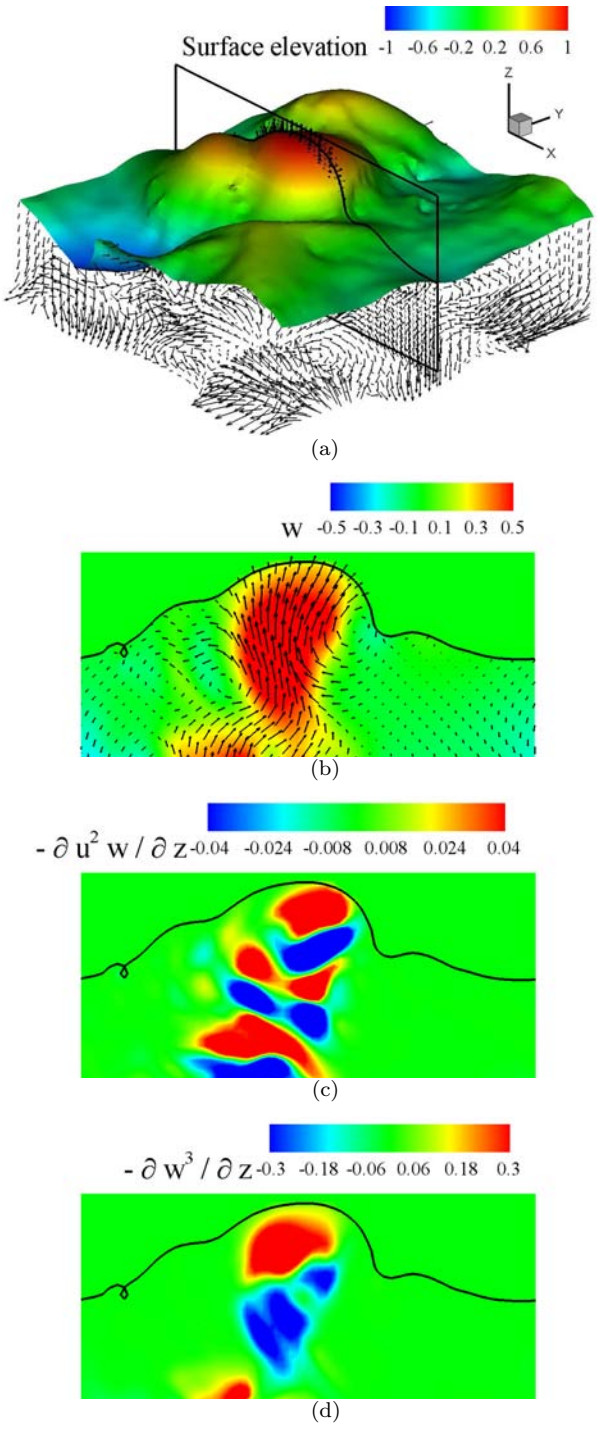

Figure 17: Instantaneous flow structure for the case of ($Fr^2 = 32, We = \infty$): (a) free surface and velocity vectors; and on a vertical cross-section, distributions of (b) vertical velocity; (c) transport of horizontal turbulent normal stress by the vertical turbulent velocity; (d) transport of vertical turbulent normal stress by the vertical turbulent velocity.

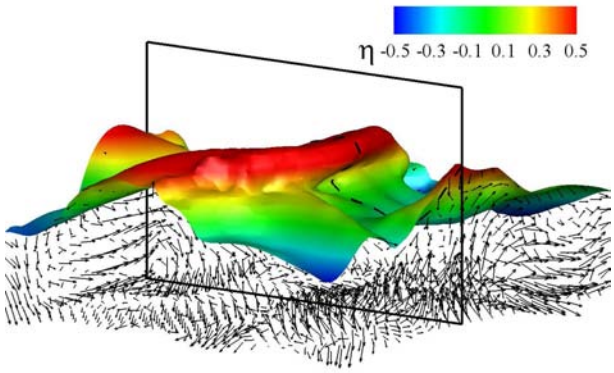

(a)

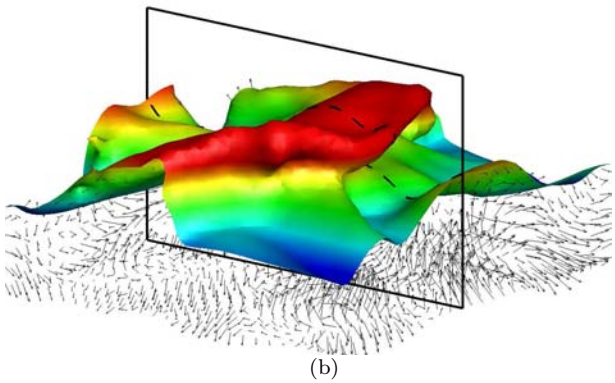

(b)

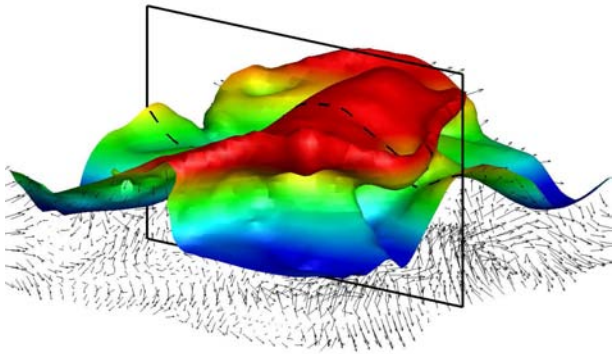

(c)

Figure 18: A surface breaking process in the case of ($Fr^2 = 16, We = \infty$). (a) A water sheet is brought up and begins to overturn. (b) The water sheet plunges downward to the free surface. (c) The water sheet reenters and then splashes up. Surface elevation contours and the velocity vectors of water are plotted. A vertical cut is extracted for analysis in Fig.19.

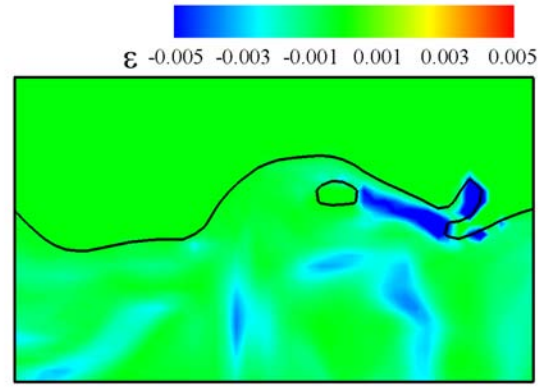

(a)

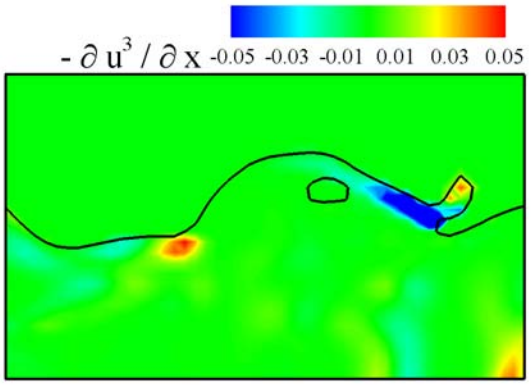

(b)

Figure 19: Energy dissipation and turbulent Reynolds stress transport associated with surface breaking: (a) viscous dissipation rate; (b) horizontal transport of the horizontal turbulent normal stress.

the wave motion is plotted in Fig.21. The production exists mainly in the viscous layer, where the dynamic free surface boundary condition is felt (Shen et al., 1999). The influence of wave motion on the horizontal stress is more significant than that on the vertical stress.

4 CONCLUSIONS

In this study, we perform a systematic study on the canonical problem of homogeneous turbulence interacting with a free surface. With the recently developed simulation capability that combines the strengths of several free-surface flow simulation tools, we are able to obtain an accurate description of the free surface and the turbulence flow field. Such infor-

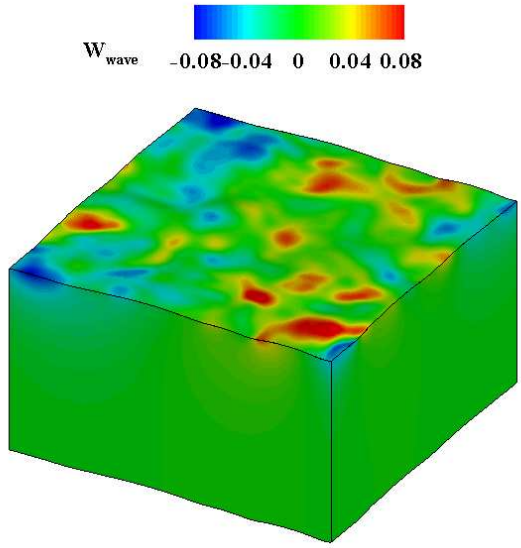

(a)

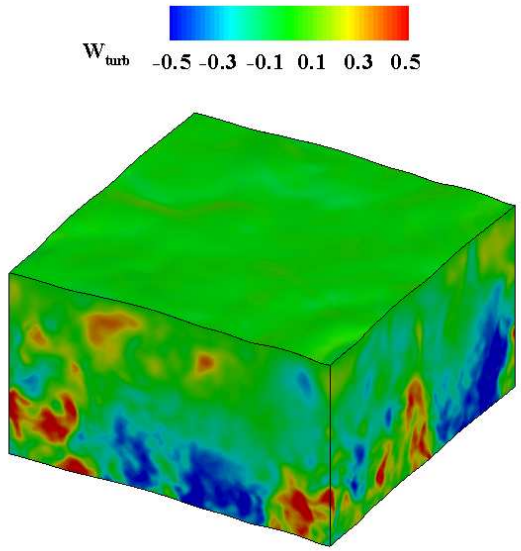

(b)

Figure 20: Helmholtz decomposition of the vertical velocity for the case of ($Fr^2 = 0.8$, $We = 40$): (a) w_{wave}, the vertical velocity component of the irrotational part of flow field; (b) w_{turb}, the vertical velocity component of the solenoidal part of the flow field.

mation is important for the modeling of free-surface turbulence.

Different flow regimes are demonstrated by the instantaneous surface geometries of representative cases. The surface elevation spectrum also demonstrates large difference among flows under different gravity and surface tension effects. We identify

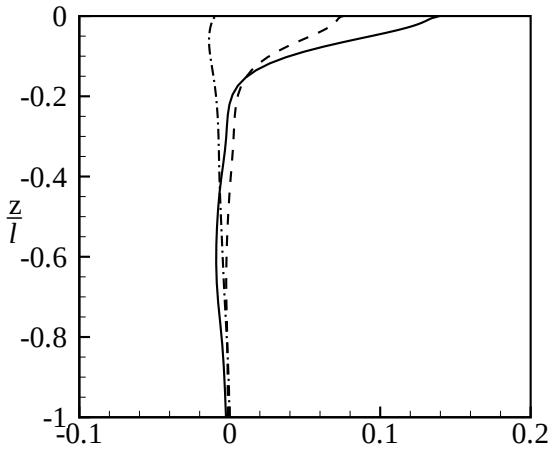

Figure 21: Turbulence production by the wave motion (normalized by q^3/l): —— , the total turbulence production from the wave; – – – , the horizontal turbulent stress production from the wave; – · – · – , the vertical turbulent stress production from the wave.

surface waves and turbulence induced surface roughness in the normalized frequency–wavenumber spectrum. The turbulence roughness is dominant at small spatial scales. The intermittency factors for violent surface cases are calculated. An equivalent intermittency layer thickness is defined based on the intermittency factors, and is discussed for different Froude and Weber numbers.

We also investigate the influence of the gravity and surface tension effects on the turbulence statistics. The blockage effect of the free surface turns the vertical motion into horizontal motion. It is strongly dependent on the Froude number and the Weber number. The smaller the Froude number and the Weber number are, the stronger the blockage effect is. The phase averaged Reynolds stress is discussed and it is determined by both the intermittency factor and the turbulent velocity fluctuation magnitude.

The two most important flow structures in SFST, namely splat and surface breaking, are also discussed. Splat is the major mechanism that turns vertical motion to horizontal motion. Strong splats generate surface breaking, and surface breaking enhances dissipation and turbulence transport significantly. Finally, a scheme for the identification of wave and turbulence motions from their complex coupled flow fields is presented. It is found that the turbu-

lence production by the wave motion exists mainly in the viscous layer.

References

[1] V. Borue, S. A. Orzag, and Staroselsky, *Interaction of surface waves with turbulence: direct numerical simulations of turbulent open-channel flow*, J. Fluid. Mech. **286** (1995), 1–23.

[2] M. Brocchini and D. H. Peregrine, *The dynamics of strong turbulence at free surfaces. part 1. description*, J. Fluid Mech. **449** (2001), 225–254.

[3] X. Guo and L. Shen, *On the generation and maintenance of waves and turbulence in simulations of free-surface turbulence*, J. Comput. Phys. **228** (2009), 7313–7332.

[4] X. Guo and L. Shen, *Interaction of a deformable free surface with statistically-steady homogeneous turbulence*, J. Fluid Mech. (in press) (2010).

[5] M. Kang, R. P. Fedkiw, and X. Liu, *A boundary condition capturing method for multiphase incompressible flow*, J. Sci. Comput. **15** (2000), no. 3, 323–360.

[6] E. Labourasse, D. Lacanette, A. Toutant, P. Lubin, S. Vincent, O. Lebaigue, J.-P. Caltagirone, and P. Sagaut, *Interface-turbulence interactions in large-scale bubbling processes*, Int. J. Multiphase Flow **33** (2007), 1–39.

[7] P. Liovic and D. Lakehal, *Interface-turbulence interactions in large-scale bubbling processes*, Int. J. Heat & Fluid Flow **28** (2007), 127–144.

[8] X. Liu, R. P. Fedkiw, and M. Kang, *A boundary condition capturing method for poisson's equation on irregular domain*, J. Comput. Phys. **160** (2000), 151–178.

[9] S. Reboux, P. Sagaut, and D. Lakehal, *Large-eddy simulation of sheared interfacial flow*, Phys. Fluid **18** (2006), no. 105105.

[10] W. J. Rider and D. B. Kothe, *Reconstructing volume tracking*, J. Comput. Phys. **141** (1998), 112–152.

[11] C. Rosales and C. Meneveau, *Linear forcing in numerical simulations of isotropic turbulence: Physical space implementations and convergence properties*, Phys. Fluids **17** (2005), no. 095106.

[12] L. Shen, *Physics of free-surface turbulence and challenges to LES, in Monograph: CFD of Multifluid FLows*, von Karman Institute, von Karman Institute, 2007.

[13] L. Shen and D.K.P. Yue, *Large-eddy simulation of free-surface turbulence*, J. Fluid Mech. **440** (2001), 75–116.

[14] L. Shen, X. Zhang, D. K. P. Yue, and G. S. Triantafyllow, *The surface layer for free-surface turbulent flows*, J. Fluid Mech. **386** (1999), 167–212.

[15] M. Sussman, E. Fatemi, P. Smereka, and S. Osher, *An improved level set method for incompressible two-phase flows*, Computers & Fluids **27** (1998), no. 5-6, 663–680.

[16] M. Sussman and E. G. Puckett, *A coupled level set and volume-of-fluid method for computing 3D and axisymmetric incompressible two-phase flows*, J. Comput. Phys. **162** (2000), 301–337.

[17] M. Sussman, P. Smereka, and S. Osher, *A level set approach for computing solutions to incompressible two-phase flow*, J. Comput. Phys. **114** (1994), 146–159.